Computers, Materials & Continua

Tech Science Press

https://doi.org/10.32604/cmc.2026.079905

ARTICLE

Tunable Optoelectronic and Thermoelectric Properties of Ag/Ga-Doped PbS Surfaces: A DFT Study on Doping and Surface Engineering

Muhammad Jawad[1], Muhammad Mudassir Ahmad Alwi[2,*], Akbar Niaz[2], Monaf Hodhod[3], Noor ul Amin[4] and Fiaz Hussain[5,*]

[1]Faculty of Science Education, Jeju National University, Jeju, Republic of Korea
[2]Department of Materials Engineering, College of Engineering, King Faisal University, Al-Hofuf, Al-Ahsa, Saudi Arabia
[3]Department of Mechanical Engineering, College of Engineering, King Faisal University, Al-Hofuf, Al-Ahsa, Saudi Arabia
[4]Department of Chemistry, Abdul Wali Khan University Mardan, Mardan, Pakistan
[5]Department of Mechanical Engineering, Gachon University, Seongnam-si, Gyeonggi-do, Republic of Korea

*Corresponding Authors: Muhammad Mudassir Ahmad Alwi. Email: malwi@kfu.edu.sa; Fiaz Hussain. Email: fiaz415@gachon.ac.kr

Received: 30 January 2026; Accepted: 13 May 2026; Published: 15 June 2026

ABSTRACT: Lead sulfide (PbS) is a narrow bandgap IV–VI semiconductor with important applications in infrared optoelectronics and thermoelectric energy conversion. Surface engineering and controlled doping provide effective strategies for tuning its electronic and optical properties. In this work, the structural, electronic, optical, and thermoelectric properties of bulk PbS, pristine PbS (110) surfaces, and Ga- and Ag-doped PbS (110) surfaces are systematically investigated using density functional theory within the full-potential linearized augmented plane wave framework. The calculated lattice constant of bulk PbS is 5.88 Å, which agrees well with experimental data. Electronic structure calculations show that bulk PbS exhibits a direct bandgap of 0.75 eV at the L point. The pristine PbS (110) surface shows an enlarged bandgap of 1.07 eV due to surface quantum confinement. Surface doping strongly modifies the electronic structure. Ag doping increases the bandgap to 1.24 eV through donor-like states, whereas Ga doping slightly reduces it to 1.01 eV by introducing acceptor states near the valence band. These electronic modifications lead to significant changes in optical behavior, including enhanced absorption in the visible and near-infrared regions and tunable dielectric response. Thermoelectric analysis reveals that the pristine surface exhibits a high power factor of approximately 4.0×10^{11} W/m·K^2 at 300 K, while bulk PbS reaches a maximum value of 4.7×10^{11} W/m·K^2 at 800 K. These results demonstrate that dopant-induced band modulation and surface engineering provide an effective approach for tuning the optoelectronic and thermoelectric performance of PbS-based nanostructures for advanced energy and photonic applications.

KEYWORDS: PbS surface; optoelectronic properties; Ga and Ag doping; DFT; thermoelectric properties

1 Introduction

IV–VI semiconductors have gained strong attention because of their unique electronic characteristics and thermal performance [1,2]. These materials show a useful combination of narrow bandgap, high carrier mobility, and low lattice thermal conductivity [3–5]. Such features make them suitable for optoelectronic and thermoelectric applications. Among them, lead chalcogenides are widely studied [4,5]. In particular, lead sulfide (PbS) has emerged as an important material for infrared devices, photovoltaics, and energy conversion systems [6–8].

PbS crystallizes in a rock-salt structure and exhibits a direct bandgap at the L-point [9,10]. Its properties can be tuned in several ways. These include size reduction, surface modification, and chemical doping [11,12].

At the nanoscale, surface effects become dominant. They strongly influence charge transport and optical absorption [13,14]. As a result, surface engineering plays a key role in controlling material performance [11–14].

Among different method, doping is used to modify semiconductor properties [15,16]. In PbS, dopants can introduce new electronic states near the band edges. This changes the carrier concentration and transport behavior. It can also affect optical transitions [17]. Many studies have reported doping effects in bulk PbS. However, surface doping is still not well explored. This creates a clear research gap.

Surface doping is important because it directly affects the local electronic structure. It can modify band alignment and charge distribution. These changes influence device efficiency [18]. The (110) surface of PbS is known to be stable and relevant for practical applications. Despite this, detailed studies on doped PbS (110) surfaces are limited. A systematic understanding is still missing.

The type of dopant plays an important role in estimating the final properties [19]. In this work, gallium (Ga) and silver (Ag) are selected as dopants. These elements show different electronic behavior. Ga usually acts as an acceptor dopant. It mainly affects the valence band and hole concentration [20]. On the other hand, Ag can introduce donor-like states. It often modifies the conduction band and optical response [21]. This contrast allows a clear comparison of doping effects.

The combined effect of surface structure and doping is particularly important. It can lead to significant changes in the density of states, bandgap, and carrier dynamics [17]. These factors are directly linked to optoelectronic and thermoelectric performance. Therefore, studying both aspects together provides deeper insight.

In this work, we investigate bulk PbS, pristine PbS (110) surfaces, and Ga- and Ag-doped PbS (110) surfaces. The focus is on understanding how doping and surface engineering influence the electronic, optical, and thermoelectric properties. The goal is to provide a clear picture of structure–property relationships. These results can help in designing improved PbS-based materials for future optoelectronic and energy applications.

2 Computational Methodology

All first-principles calculations in the present research work were attained using the full-potential linearized augmented plane wave (FP-LAPW) method as employed with in the WIEN2k code [22]. The electronic characteristics was calculated within the framework DFT [23,24], and the exchange-correlation effects were treated using the generalized gradient approximation (GGA) in the Perdew-Burke-Ernzerhof (PBE) form [25]. This computational methodology has been widely utilized for studying the optoelectronic and structural properties of semiconducting chalcogenide materials [10,26].

In the FP-LAPW scheme, the crystal space is divided into non-overlapping muffin-tin spheres around the atomic sites and an interstitial region between them [22]. Inside the muffin-tin spheres, the wave functions were expanded in spherical harmonics up to $l_{max} = 10$, while plane waves were used in the interstitial region. The basis-set size was controlled by the parameter $R_{MT}K_{max} = 7$, which is sufficient to ensure numerical convergence of the calculated properties. The muffin-tin radii were selected carefully in order to avoid overlap between neighboring spheres and to minimize charge leakage from the atomic core regions.

The Brillouin-zone integrations were carried out using the Monkhorst-Pack k-point sampling method [27]. For bulk PbS, approximately 1000 k-points in the irreducible Brillouin zone were used to achieve good convergence of the total energy. The self-consistent field calculations were considered converged when the total energy difference between successive iterations was less than 10^{-4} Ry. Structural optimization was performed by minimizing both the total energy and the atomic forces. The convergence criteria for geometry relaxation were set to 1×10^{-5} eV for the total energy and 0.01 eV/Å for the atomic forces.

To model surface effects, the PbS (110) surface was constructed using a periodic supercell approach [28,29]. Substitutional doping was introduced by replacing one Pb atom in the surface supercell with either Ag or Ga, allowing us to investigate the dopant-induced changes in the structural, electronic, optical, and thermoelectric properties of the system [26,30]. The electronic band structure and density of states were calculated for the optimized structures, while the optical response was obtained from the complex dielectric function derived from the electronic transitions within the DFT framework as evidenced by the recent literature [31,32]. In addition, the thermoelectric transport properties, including the Seebeck coefficient, electrical conductivity, and thermal conductivity, were evaluated as a function of temperature in order to assess the thermoelectric performance of the pristine and doped PbS systems by using the BoltzTraP code [33].

3 Surface Models

At room temperature, PbS crystallizes in the rock-salt cubic structure belonging to the Fm3m space group, which is characteristic of many IV–VI semiconductor compounds [10,26]. This crystal structure has been extensively investigated both experimentally and theoretically due to its importance in optoelectronic and thermoelectric applications.

To investigate surface-dependent phenomena, the (110) and (111) surfaces of PbS-recognized as thermodynamically stable and technologically relevant facets-were constructed using a periodic slab supercell approach. Surface modeling is essential for understanding the electronic and optical behavior of semiconductor nanostructures, as reduced dimensionality and broken symmetry at the surface can significantly modify the band structure and carrier dynamics. The structural configurations of the modeled PbS surfaces are illustrated in Fig. 1.

The supercell construction ensures periodic boundary conditions in the in-plane directions, while a sufficiently large vacuum layer was introduced perpendicular to the surface to avoid artificial interactions between periodic slabs. This approach is commonly employed in first-principles simulations to accurately describe surface relaxation and electronic reconstruction in semiconductor materials. Surface modeling is particularly important for capturing quantum confinement and surface-state effects, which strongly influence the optical absorption and electronic transport properties of nanoscale PbS systems.

To evaluate doping-induced modifications, substitutional doping was introduced by replacing Pb atoms with Ga or Ag dopant atoms in the optimized surface supercells. This strategy allows a systematic investigation of how heteroatom incorporation modifies the local atomic environment, charge distribution, and electronic structure of the PbS surfaces. Such substitutional doping approaches have been widely used in first-principles studies to analyze dopant-induced band structure engineering and surface reactivity in semiconductor materials [30].

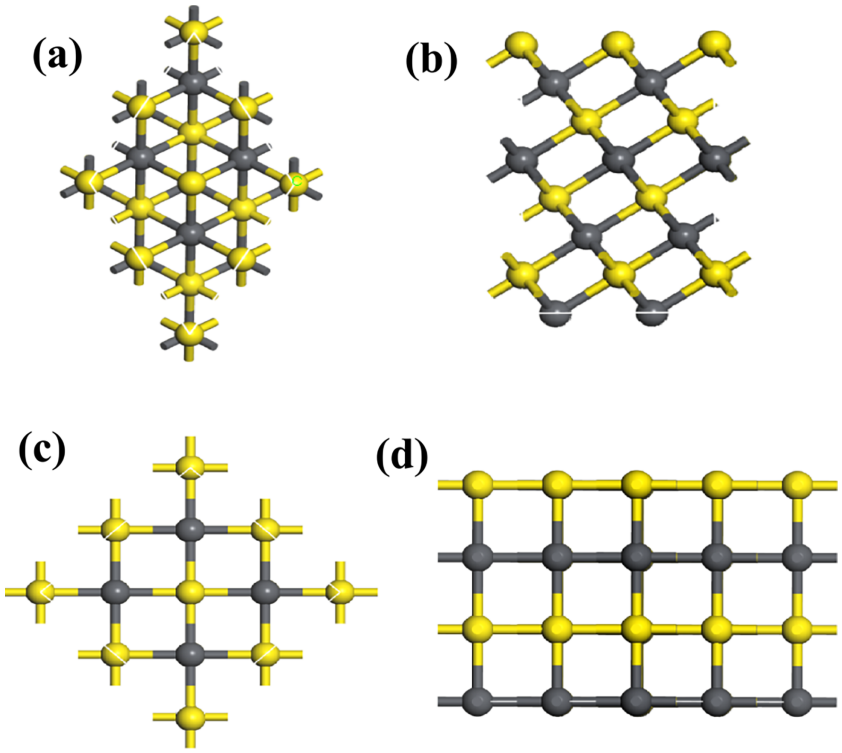

Figure 1: Crystal structure of PbS showing the (**a**,**c**) top view and (**b**,**d**) side view of (110) and (111) surface. Grey spheres represent Pb atoms and yellow spheres represent S atoms.

4 Results and Detailed Discussions

4.1 Structural Properties

To validate the computational methodology employed in this study, we first optimized the bulk PbS structure and calculated its lattice parameters. The resulting lattice constant of 5.88 Å shows good agreement with previously reported experimentally and theoretically attained values for PbS, confirming the reliability of the computational framework [34].

As outlined previously, the (110) and (111) surfaces of PbS were systematically modeled. Structural optimization was performed prior to the calculation of optoelectronic properties to ensure that the systems correspond to their ground-state energy configurations, which is essential for reliable electronic structure predictions. Geometry relaxations were carried out using the Perdew–Burke–Ernzerhof generalized gradient approximation (GGA-PBE) functional, with atomic forces minimized below 0.01 eV/Å and energy convergence set to 1×10^{-5} eV/atom. The optimized bulk PbS structure, illustrated in Fig. 2, retains its cubic symmetry with negligible structural distortion.

Comparative analysis of the modeled surfaces indicates that the (110) surface is the most thermodynamically stable configuration, which is consistent with previous theoretical studies on PbS surfaces and related rock-salt semiconductors. Consequently, the subsequent analysis in this work focuses on the (110) surface to investigate the influence of Ga and Ag doping on the electronic and optical properties.

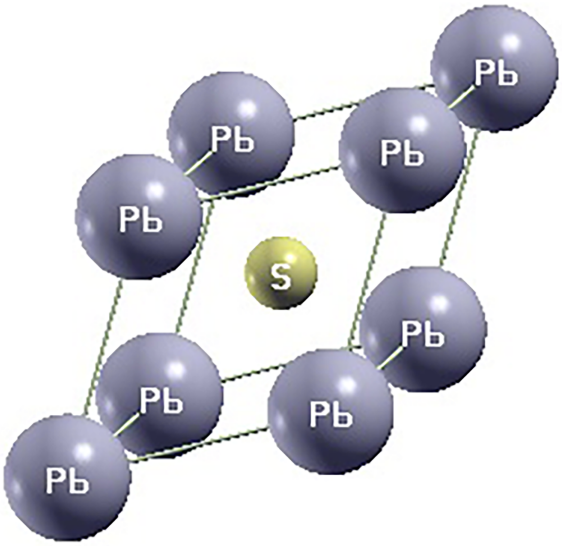

Figure 2: Optimized crystal structure of bulk PbS.

4.2 Band Structure

The calculation of electronic band structures is essential for understanding the fundamental electronic characteristics of materials, which also includes their stability, optical behavior, and bandgap characteristics. In particular, band structure analysis allows determination of the nature of the bandgap-whether direct or indirect-which strongly influences the optoelectronic performance of semiconductor materials [15,16].

The electronic band structures of PbS systems-bulk, pristine (110) surface, and Ga/Ag-doped (110) surfaces-were systematically investigated to understand their semiconducting behavior and bandgap tunability. Fig. 3 shows the estimated band structure of our understudy compounds along the high-symmetry brilloiun zone directions, with the Fermi level (E_F) at 0 eV. The estimated bandgaps for bulk PbS, pristine (110) surface, Ag-doped, and Ga-doped surfaces are 0.75, 1.07, 1.24, and 1.01 eV, respectively (Fig. 3), confirming the semiconducting nature of all systems. The calculated bulk bandgap agrees well with previously reported theoretical values for PbS (0.73–0.78 eV), which validates the reliability of the computational method used in this work [26].

For bulk PbS, the valence band maximum (VBM) and conduction band minimum (CBM) are located at the L-high symmetry point, which indicates a direct bandgap semiconductor (Fig. 3a) [34]. This direct transition is beneficial for optoelectronic applications because it allows efficient optical absorption and electron–hole recombination processes. In contrast, the pristine (110) surface exhibits a slightly larger bandgap (1.07 eV) and an indirect transition, where the VBM shifts toward the Γ-point while the CBM remains at L (Fig. 3b). Such modifications in the electronic structure arise from surface effects and reduced dimensionality, which alter orbital hybridization and the electronic state distribution near the E_F in low-dimensional systems [13,14].

The introduction of dopant atoms leads to noticeable changes in the electronic structure. Ag doping increases the bandgap to 1.24 eV, whereas Ga doping reduces it to 1.01 eV, while maintaining the semiconducting behavior of the system (Fig. 3c,d). In the Ag-doped system, the conduction band shifts upward due to the presence of Ag-derived electronic states, resulting in a wider effective bandgap. Conversely, Ga doping introduces additional states near the valence band region, which slightly reduces the bandgap. These results

demonstrate that dopant incorporation significantly modifies the electronic structure and band alignment of PbS surfaces [17,18,26].

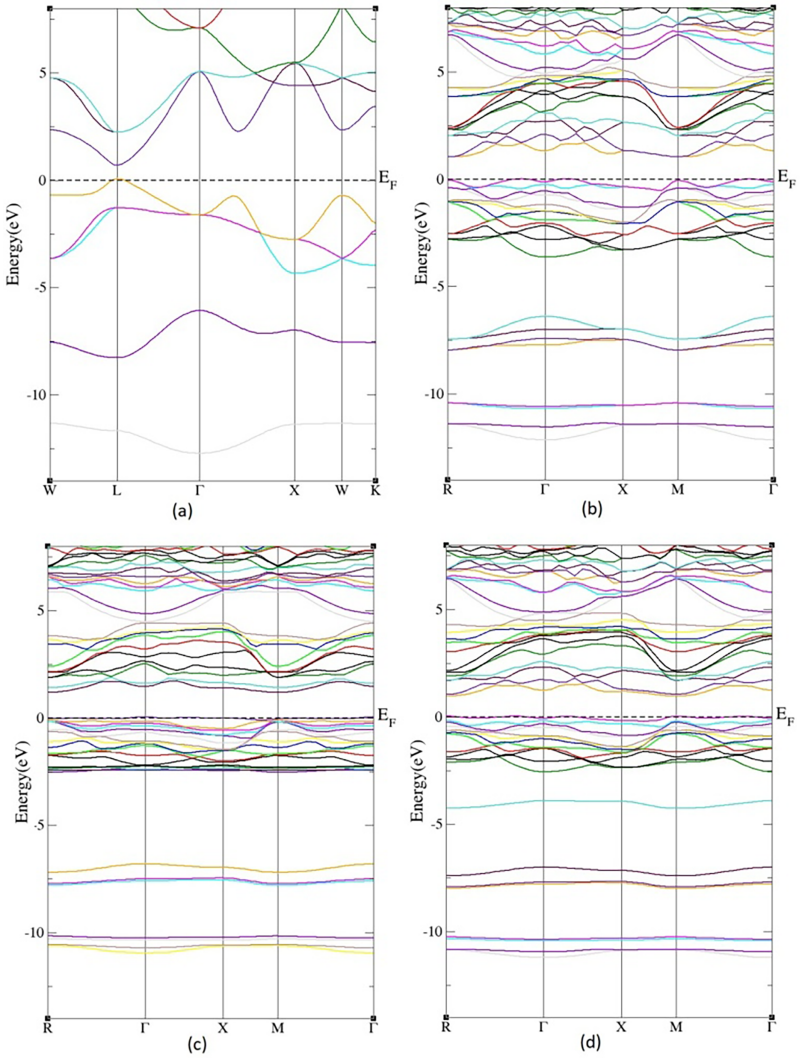

Figure 3: Band structure of (**a**) Bulk PbS (**b**) Pristine PbS (110) (**c**) Ag doped PbS (110) (**d**) Ga doped PbS (110).

Overall, the ability to tune the bandgap through surface modification and substitutional doping highlights the versatility of PbS for optoelectronic applications. The observed band structure variations indicate that controlled doping can be an effective strategy for tailoring the electronic properties of PbS-based materials for devices such as infrared photodetectors and photovoltaic absorbers.

4.3 Density of States

The investigation of density of states (DOS) is very important for understanding the electronic structure of materials, as it describes the electronic states distribution along different energy levels [34]. In this work, both the partial density of states (PDOS) and total density of states (TDOS) were computed for the bulk PbS, pristine (110) surfaces, and Ag/Ga-doped (110) surfaces (Figs. 4 and 5). All spectra are referenced to the Fermi level (E_F = 0 eV), where the regions $E < E_F$ and $E > E_F$ correspond to the valence and conduction

bands, respectively. The TDOS profiles (Fig. 4) confirm the presence of narrow bandgaps in all systems, consistent with their semiconducting behavior and applicability for optoelectronic device applications. Bulk PbS exhibits the smallest bandgap (0.75 eV), whereas the Ag-doped (110) surface shows the largest bandgap (1.24 eV). Surface effects leads to an increase inDOS near the E_F, particularly in the Ag-doped system where pronounced peaks appear in both the valence and conduction regions. This behavior can be attributed to surface-induced electronic localization and dopant-related states [17,18].

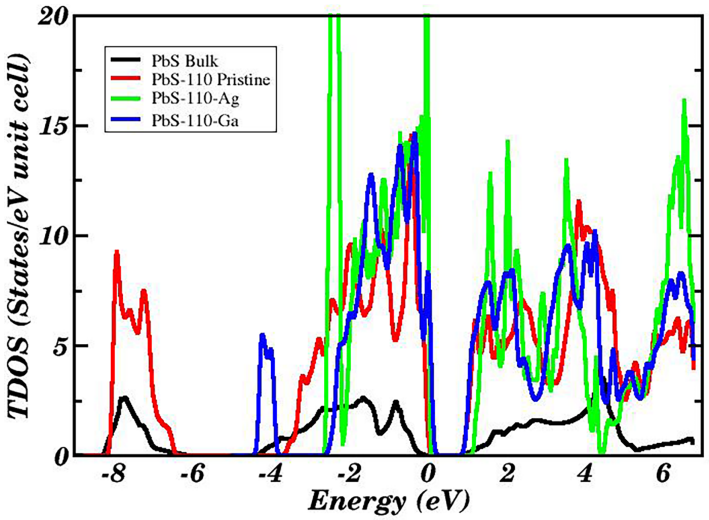

Figure 4: Calculated total density of states (TDOS) for bulk, pristine and doped PbS surfaces.

A secondary gap observed around −6 to −5.5 eV appears in all configurations. This feature originates from hybridization between Pb-6s and S-3p orbitals, reflecting the intrinsic bonding characteristics of the rock-salt crystal structure of PbS [34].

For bulk PbS (Fig. 5a), the valence band is mainly consists of Pb-6s and S-3p orbitals, while the conduction band is dominated by S-3p and Pb-6p states. These orbital contributions are consistent with previous theoretical studies of lead chalcogenides. In the pristine (110) surface (Fig. 5b), the valence band shows increased contribution from S-3s states at lower energies (−8 to −6 eV), while Pb-6p and S-3p states overlap near the Fermi level, indicating enhanced surface electronic activity.

In the Ag-doped surface (Fig. 5c), the contribution from lower-energy S-3s states decreases and the spectral weight shifts toward the conduction region. Ag-derived states interact with Pb-6p orbitals in the energy range of 2–4 eV, leading to the formation of hybridized electronic states that contribute to charge transport. In contrast, Ga doping (Fig. 5d) introduces additional Ga-4p states near −4 eV, which interact more weakly with the host orbitals and slightly reduce the bandgap (1.01 eV). This weaker hybridization suggests that Ga behaves as an acceptor-type dopant, while Ag introduces donor-like electronic states.

Overall, the DOS results demonstrate that surface modification and substitutional doping significantly alter the electronic structure of PbS. The increased density of states near the Fermi level in Ag-doped surfaces may enhance carrier transport properties, whereas Ga doping maintains semiconducting behavior with moderate bandgap reduction. These results further illustrate the potential of controlled doping for tuning the electronic properties of PbS surfaces for optoelectronic and energy-related applications [17,20].

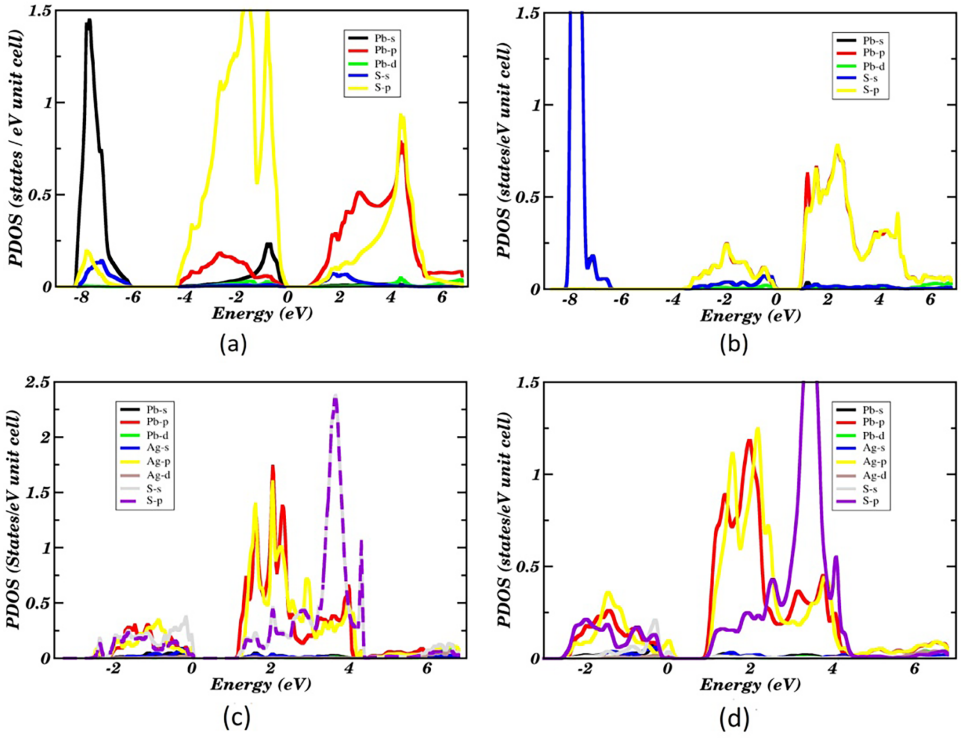

Figure 5: Calculated partial density of states (PDOS) for (**a**) bulk (**b**) clean 110 (**c**) Ag doped 110 and (**d**) Ga doped 110 surface.

4.4 Optical Properties

The optical behavior of a semiconductor is closely relevant to its electronic structure. Changes in band structure and density of states directly influence interband transitions and therefore modify optical absorption and dielectric response [31,32]. Since the previous sections demonstrated that Ga and Ag doping significantly alter the electronic-structure of PbS (110) surfaces, it is important to examine how these modifications affect their optical properties. Consequently, the optical response of bulk PbS, pristine PbS (110), and doped PbS (110) surfaces is analyzed in the following subsections.

The optical characteristics of a material play a very important role in estimating its compatibility for optoelectronic and photovoltaic applications. These properties are typically derived from the electronic structure through the complex dielectric function, which accounts for interband electronic transitions and the joint DOS including dipole transition matrix elements. In the present work, the optical properties were calculated within the GGA framework. The complex dielectric function for bulk PbS, pristine PbS (110), Ag-doped PbS (110), and Ga-doped PbS (110) surfaces is expressed as

$$\varepsilon(\omega) = \varepsilon_1(\omega) + i\varepsilon_2(\omega)$$

here the $\varepsilon_1(\omega)$ and $\varepsilon_2(\omega)$ represent the real and imaginary parts of the dielectric function, respectively. Within the random phase approximation, interband electronic transitions determine the imaginary component of the dielectric response, while the real component is obtained through the Kramers–Kronig relations. From the dielectric function, several optical constants including refractive index, reflectivity, energy loss spectrum, absorption coefficient, and extinction coefficient can be derived.

4.5 Complex Dielectric Function

The complex dielectric function gives important information about the optical and electronic response of PbS systems. Fig. 6 shows the calculated real $\varepsilon_1(\omega)$ and imaginary $\varepsilon_2(\omega)$ components for bulk PbS, pristine (110) surfaces, and Ag/Ga-doped (110) surfaces [31].

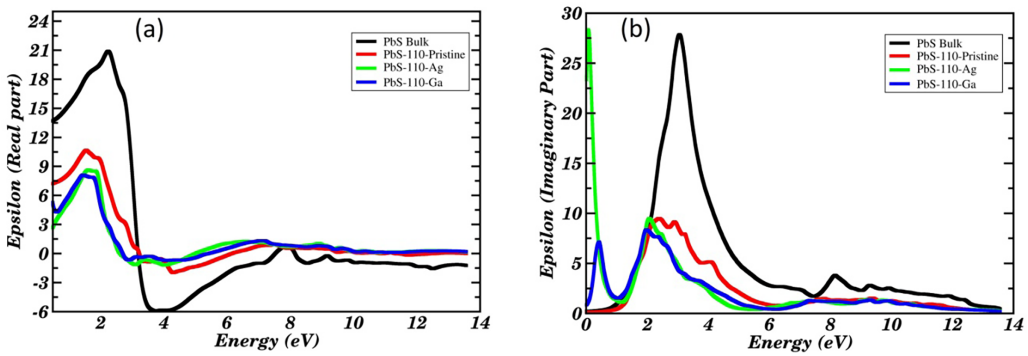

Figure 6: Calculated (**a**) real and (**b**) imaginary parts for bulk, pristine and doped PbS surfaces.

The real dielectric function (Fig. 6a) represents the polarizability and electronic screening capability of the material. For all systems, $\varepsilon_1(\omega)$ initially increases within the low-energy region before reaching a maximum near 2.5 eV, followed by a gradual decrease. Bulk PbS shows negative $\varepsilon_1(\omega)$ values between approximately 3–14 eV, which is associated with plasmon-related collective electronic oscillations above the plasma frequency. Similar behavior is also observed for the surface systems in the 3–5 eV region, indicating surface-related electronic transitions.

The static dielectric constant $\varepsilon_1(0)$ is smallest for the Ag-doped surface, suggesting weaker electronic screening. Materials with lower dielectric constants often exhibit reduced capacitive losses and improved carrier transport behavior in high-frequency electronic devices.

The imaginary dielectric function $\varepsilon_2(\omega)$ (Fig. 6b) describes optical absorption arising from interband transitions. The onset of absorption corresponds closely to the calculated bandgap energies (0.75–1.24 eV). Strong absorption peaks occur between the bandgap and 4 eV, which mainly originate from transitions between S-3p valence states and Pb-6p conduction states [30]. The decrease in $\varepsilon_2(\omega)$ beyond 4 eV indicates reduced optical transitions and increasing transparency in the ultraviolet region.

The calculated dielectric responses demonstrate that doping and surface modification significantly influence the optical behavior of PbS systems. Such tunable optical properties are desirable for applications in infrared photodetectors, optoelectronic devices, and photovoltaic absorbers.

4.6 Absorption Coefficient

The absorption coefficient describes the ability of a material to absorb incident electromagnetic radiation. Fig. 7 presents the calculated absorption spectra for bulk PbS, pristine (110) surfaces, and Ag/Ga-doped (110) surfaces within the 0–14 eV energy range [26,32].

The absorption onset corresponds closely to the calculated bandgap values (0.75–1.24 eV), confirming the semiconducting nature of all systems. A broad absorption region between 1–4 eV is observed for all configurations, which is attributed to electronic transitions from S-3p valence states to Pb-6p conduction states. In doped systems, additional contributions from Ag-4p and Ga-4p orbitals slightly broaden the absorption spectrum [21].

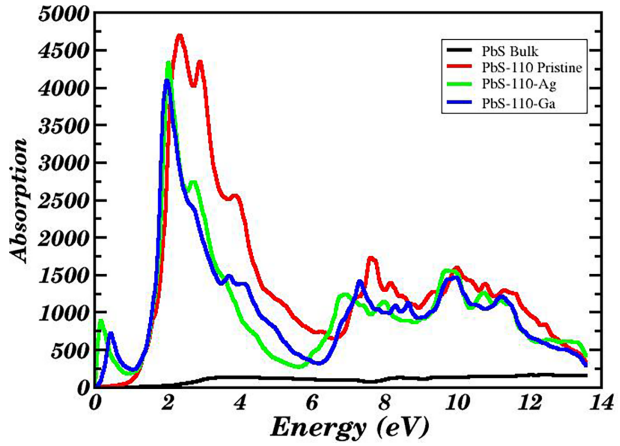

Figure 7: Calculated absorption coefficient for bulk, pristine and doped PbS surfaces.

The absorption intensity decreases beyond 4 eV, indicating reduced electronic transitions and increasing transparency in the ultraviolet region. These characteristics suggest that PbS and its doped surfaces possess suitable optical absorption properties for photovoltaic and infrared optoelectronic applications.

4.7 Refractive Index

The refractive index n(ω) is an important optical parameter that determines the propagation of electromagnetic waves within a material. Fig. 8 shows the calculated refractive index spectra for bulk PbS, pristine (110) surfaces, and doped surfaces.

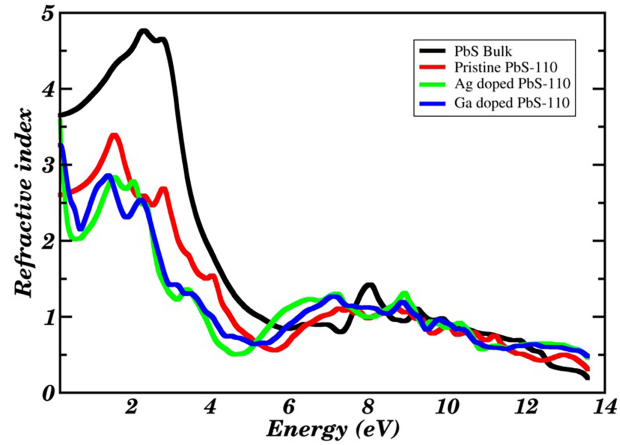

Figure 8: Calculated refractive index for bulk, pristine and doped PbS surfaces.

Bulk PbS exhibits the highest refractive index across the studied energy range, reaching a maximum near 2 eV, which originates from strong interband transitions between S-3p and Pb-6p states. In contrast, the pristine and doped surfaces show lower refractive index values due to reduced electronic screening and surface effects [35,36].

The static refractive indices follow the trend:

$$n_{Ag\,doped} > n_{Ga\,doped} > n_{pristine}$$

which is consistent with the behavior of the real dielectric constant $\varepsilon_1(\omega)$. The reduced refractive index of the surface systems compared to bulk PbS can be attributed to surface-induced electronic localization and reduced atomic coordination. These optical characteristics suggest that doped PbS surfaces may be useful for photonic and optoelectronic applications such as optical sensors and integrated photonic devices.

4.8 Reflectivity

The reflectivity spectrum describes the fraction of incident light reflected from the material surface [37]. Fig. 9 illustrates the calculated reflectivity for bulk PbS, pristine (110) surfaces, and Ag/Ga-doped surfaces.

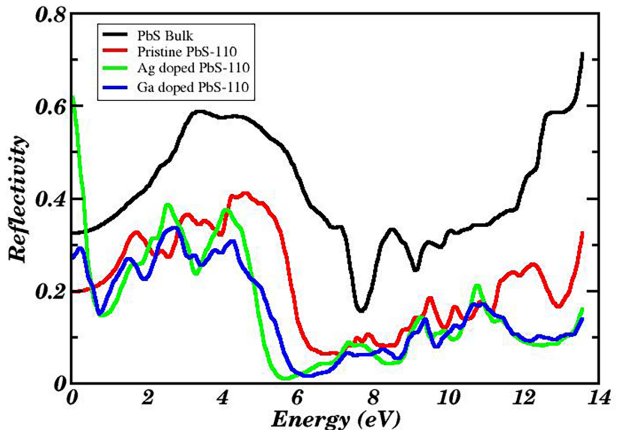

Figure 9: Calculated reflectivity for bulk, pristine and doped PbS surfaces.

For all systems, reflectivity increases with photon energy and reaches maximum values in the ultraviolet region. Bulk PbS exhibits the highest reflectivity, while the doped surfaces show slightly lower values due to reduced electronic density near the surface. The reflectivity peaks correspond to strong interband transitions between S-3p valence states and Pb-6p conduction states, consistent with the features observed in the dielectric function spectra.

At higher energies (above 12 eV), the reflectivity increases due to collective electronic excitations and plasmon-related effects, which occur when the real dielectric function becomes negative. The lower reflectivity observed for doped surfaces indicates reduced electronic screening and enhanced photon absorption, which can be beneficial for optoelectronic device performance.

Overall, the optical analysis demonstrates that surface modification and dopant incorporation provide an effective approach for tuning the optical properties of PbS materials for applications such as infrared detectors, optical coatings, and photovoltaic devices.

5 Thermoelectric Properties

Thermoelectric materials enable the conversion of heat directly into electrical energy by employing the Seebeck effect and have attracted considerable attention for energy harvesting and waste heat recovery applications [38,39]. The thermoelectric capability of a material is mainly governed by 3 transport parameters: the electrical conductivity σ, Seebeck coefficient S, and thermal conductivity [40]. A high electrical

conductivity and Seebeck coefficient combined with low thermal conductivity are desirable for efficient thermoelectric energy conversion. In addition, the electrical contribution to thermoelectric performance is commonly evaluated through the power factor PF = $S^2\sigma$. Therefore, analyzing these transport properties provides useful insight into the thermoelectric potential of PbS-based systems.

The thermoelectric properties of PbS structures, including bulk, pristine (110) surfaces, and Ag/Ga-doped (110) surfaces, demonstrate temperature-dependent behavior governed by the interplay of electronic and thermal transport mechanisms. The Seebeck coefficient (S), which measures the voltage generated under a temperature gradient, reveals distinct trends across the studied systems. The calculated Seebeck coefficient is shown in Fig. 10. Bulk PbS exhibits a steady increase in S from ~50 μV/K at 300 K to ~200 μV/K at 800 K, driven by thermally activated carriers and reduced electron–phonon scattering at elevated temperatures [41]. Similar temperature-dependent increases in Seebeck coefficient have been reported for PbS-based thermoelectric materials in previous experimental and theoretical studies. In contrast, the pristine PbS-110 surface shows a non-monotonic response, peaking at ~200 μV/K at 300 K before declining to ~50 μV/K at 800 K. This behavior can be attributed to the influence of surface states at lower temperatures and enhanced carrier scattering at higher temperatures in reduced-dimensional systems.

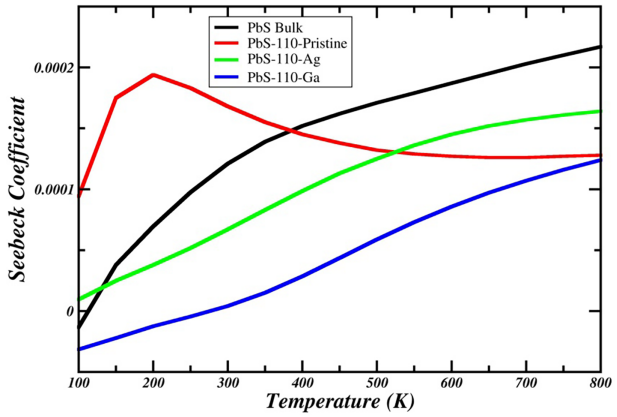

Figure 10: The calculated Seebeck coefficient for PbS bulk, pristine 110, Ag doped 110 and Ga doped 110 surface.

Doping introduces asymmetric modifications to the Seebeck response. Ag-doped PbS-110 evolves from near-zero S at 300 K to ~100 μV/K at 800 K, indicating n-type behavior due to donor states near the conduction band. In contrast, Ga-doped PbS-110 changes from negative S (~−30 μV/K at 300 K) to ~100 μV/K at 800 K, reflecting p-type conductivity induced by acceptor states near the valence band. Dopant-induced tuning of carrier type and concentration has been widely used to enhance thermoelectric performance in IV–VI semiconductor systems [42].

Electrical conductivity (σ) (Fig. 11), governed by carrier concentration and mobility, also varies significantly among the studied systems. The pristine PbS-110 surface demonstrates the highest σ, increasing from ~1.2×10^{19} S/m at 300 K to ~1.5×10^{19} S/m at 800 K. This behavior can be associated with reduced surface defects and enhanced carrier mobility in the optimized surface structure. Bulk PbS exhibits a gradual increase in σ from ~4.5×10^{18} S/m at 300 K to ~1.35×10^{19} S/m at 800 K, which is consistent with thermally activated carrier generation in narrow-bandgap semiconductors.

Doping affects the electrical conductivity differently for each dopant. Ag-doped surfaces show relatively lower σ (~5×10^{18} S/m at 300 K) due to ionized impurity scattering, with partial recovery at higher temperatures (~7×10^{18} S/m at 800 K). Ga-doped surfaces display a slight decrease in conductivity from

8×10^{18} S/m at 300 K to 7×10^{18} S/m at 800 K, which is typical for p-type systems where hole–phonon scattering becomes more significant at elevated temperatures.

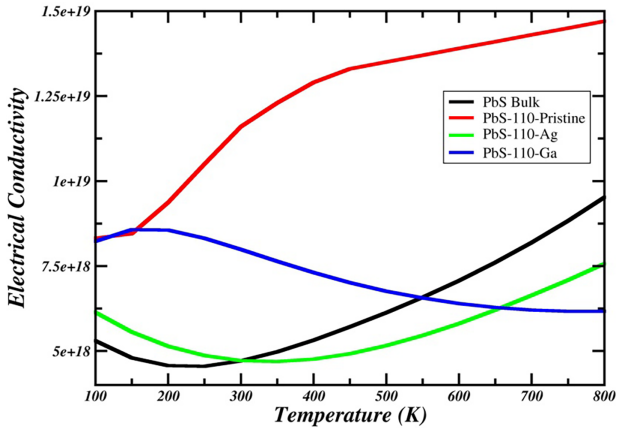

Figure 11: The calculated electrical conductivity for PbS bulk, pristine 110, Ag doped 110 and Ga doped 110 surface.

Thermal conductivity (κ) is another key parameter controlling thermoelectric efficiency because it determines heat transport through the material. Efficient thermoelectric materials typically require low thermal conductivity to maintain a temperature gradient across the material. As shown in Fig. 12, Bulk PbS exhibits the highest κ, increasing from ~1×10^{14} W/m·K at 300 K to ~5.8×10^{14} W/m·K at 800 K, primarily dominated by lattice vibrations and phonon transport. The pristine PbS-110 surface shows intermediate κ values (~0.5–4.8×10^{14} W/m·K). Doped systems display further reduction in κ due to enhanced phonon scattering introduced by dopant atoms and lattice distortions.

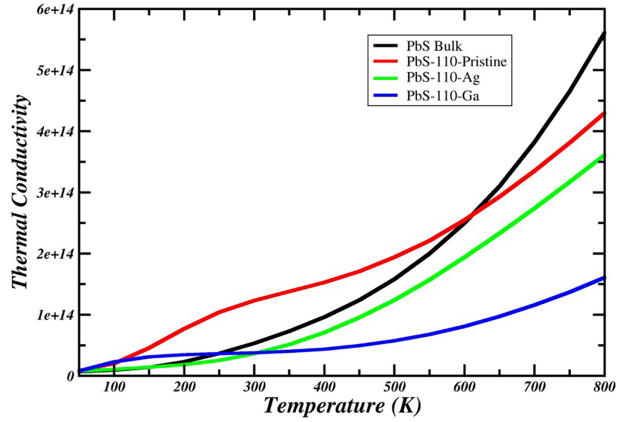

Figure 12: The calculated thermal conductivity for PbS bulk, pristine 110, Ag doped 110 and Ga doped 110 surface.

Specifically, Ag-doped surfaces reach ~3.9×10^{14} W/m·K at 800 K, while Ga-doped surfaces exhibit the lowest κ (~2.1×10^{14} W/m·K at 800 K). The reduction in thermal conductivity can be attributed to mass fluctuation scattering and increased phonon–defect interactions caused by dopant atoms. Such suppression of thermal conductivity follows the well-known "phonon-glass electron-crystal" concept, where phonon transport is reduced without significantly degrading electrical transport properties.

The power factor PF = $S^2\sigma$ [43], which combines electrical conductivity and Seebeck coefficient, provides a useful measure of thermoelectric performance. Bulk PbS achieves the highest PF at 800 K

(~4.7 × 10^{11} W/m·K^2), benefiting from simultaneous increases in S and σ at elevated temperatures (Fig. 13). The pristine PbS-110 surface reaches its maximum PF (~4.0 × 10^{11} W/m·K^2) at 300 K but decreases at higher temperatures, indicating better suitability for low-temperature thermoelectric applications.

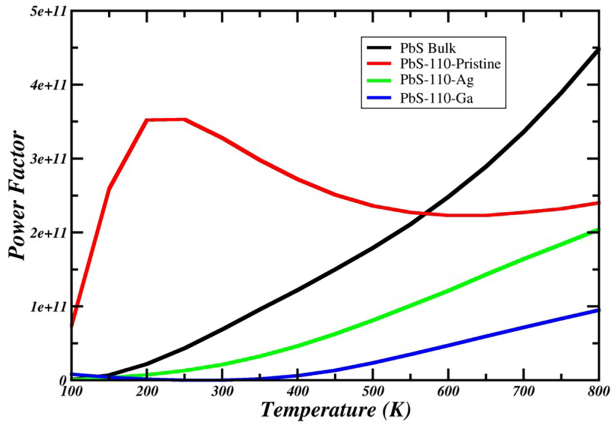

Figure 13: The calculated power factor for PbS bulk, pristine 110, Ag doped 110 and Ga doped 110 surface.

Doped systems show gradual improvement with increasing temperature. Ag-doped surfaces increase from negligible PF values to ~2.2 × 10^{11} W/m·K^2 at 800 K, whereas Ga-doped systems reach ~1.2 × 10^{11} W/m·K^2 at 800 K. This behavior reflects the typical trade-off between Seebeck coefficient and electrical conductivity observed in thermoelectric materials.

Overall, the results indicate that bulk PbS exhibits superior thermoelectric performance at high temperatures, making it suitable for waste heat recovery applications. In contrast, the pristine surface performs better at lower temperatures, while doped PbS systems-particularly Ga-doped surfaces with reduced thermal conductivity-show potential for thermoelectric device optimization through doping and surface engineering.

6 Conclusion

In this work, the structural, electronic, optical, and thermoelectric properties of bulk PbS, pristine PbS (110) surfaces, and Ga- and Ag-doped PbS (110) surfaces were systematically investigated using density functional theory within the FP-LAPW framework. The calculated lattice constant of bulk PbS is 5.88 Å, which agrees well with experimental reports and validates the computational approach used in this study. Electronic structure analysis shows that bulk PbS exhibits a direct bandgap of 0.75 eV at the L point. The pristine PbS (110) surface displays a larger bandgap of 1.07 eV due to surface-induced quantum confinement effects. Surface doping significantly modifies the electronic structure. Ag doping increases the bandgap to 1.24 eV by introducing donor-like states, while Ga doping reduces the bandgap to 1.01 eV through acceptor states near the valence band maximum.

These electronic modifications strongly influence the optical response of the material. The calculated dielectric function, refractive index, absorption coefficient, and reflectivity indicate enhanced absorption in the visible and near-infrared energy ranges. The Ag-doped surface exhibits a relatively low static dielectric constant of approximately 3.25 and increased reflectivity at low photon energies, suggesting potential applications in high-frequency optoelectronic devices. In contrast, Ga-doped surfaces exhibit reduced thermal conductivity due to enhanced phonon scattering caused by mass mismatch between dopant and host atoms.

Thermoelectric analysis reveals that the pristine PbS (110) surface shows high electrical conductivity and achieves a power factor of approximately 4.0×10^{11} W/m·K^2 at 300 K. Bulk PbS demonstrates improved thermoelectric performance at elevated temperatures, reaching a maximum power factor of about 4.7×10^{11} W/m·K^2 at 800 K. Overall, the results demonstrate that surface engineering and dopant-induced band modulation provide an effective strategy for tuning the optoelectronic and thermoelectric performance of PbS-based nanostructures. These findings provide useful theoretical guidance for the design of PbS materials for infrared optoelectronics and thermoelectric energy conversion devices.

Acknowledgement: This work was supported by the Deanship of Scientific Research, Vice Presidency for Graduate Studies and Scientific Research, King Faisal University, Saudi Arabia.

Funding Statement: This work was supported by the Deanship of Scientific Research, Vice Presidency for Graduate Studies and Scientific Research, King Faisal University, Saudi Arabia [Grant No. KFU261212].

Author Contributions: Conceptualization and methodology were performed by Muhammad Jawad. Computational simulations, data analysis, and visualization were carried out by Muhammad Jawad and Muhammad Mudassir Ahmad Alwi. Fiaz Hussain, Akbar Niaz, Monaf Hodhod and Noor ul Amin contributed to supervision, interpretation of results, and critical revision of the manuscript. The original draft was written by Muhammad Jawad. All authors reviewed and approved the final version of the manuscript.

Availability of Data and Materials: Data will be available on reasonable request.

Ethics Approval: This research does not involve human participants, human data, or animals, and therefore ethical approval was not required.

Conflicts of Interest: The authors declare no conflicts of interest.

References

1. Zhu T. Advances in thermoelectric materials research. Small Sci. 2025;5(3):2500029. doi:10.1002/smsc.202500029.
2. Singh R, Dogra S, Dixit S, Vatin NI, Bhardwaj R, Sundramoorthy AK, et al. Advancements in thermoelectric materials for efficient waste heat recovery and renewable energy generation. Hybrid Adv. 2024;5(1):100176. doi:10.1016/j.hybadv.2024.100176.
3. Gan Y, Wang G, Zhou J, Sun Z. Prediction of thermoelectric performance for layered IV-V-VI semiconductors by high-throughput *ab initio* calculations and machine learning. npj Comput Mater. 2021;7(1):176. doi:10.1038/s41524-021-00645-y.
4. Wang J, Yin Y, Che C, Cui M. Research progress of thermoelectric materials—a review. Energies. 2025;18(8):2122. doi:10.3390/en18082122.
5. Alsalama MM, Hamoudi H, Abdala A, Ghouri ZK, Youssef KM. Enhancement of thermoelectric properties of layered chalcogenide materials. Rev Adv Mater Sci. 2020;59(1):371–8. doi:10.1515/rams-2020-0023.
6. Yin X, Zhang C, Guo Y, Yang Y, Xing Y, Que W. PbS QD-based photodetectors: future-oriented near-infrared detection technology. J Mater Chem C. 2021;9(2):417–38. doi:10.1039/d0tc04612d.
7. Wang D, Li Y, Yang Y, Ding C, Shen Q. Unveiling of efficiency limit to fabricate high-performance PbSe quantum dot solar cells. Sol Energy. 2022;247(9):432–40. doi:10.1016/j.solener.2022.10.034.
8. Hamdedein A, Aboud AA, El Rouby WA, Khan MD, Farghali AA, Khedr MH, et al. Effect of La doping on the structural and gas sensing properties of PbS thin films deposited by spray pyrolysis. IOP Conf Ser Mater Sci Eng. 2021;1046(1):012026. doi:10.1088/1757-899x/1046/1/012026.
9. Sharma DS, Patel VK, Patel HV, Patel MH. Spectroscopic investigation of tunable size PbS nanocrystals embedded in PEO matrix. Mater Today Proc. 2022;67:205–9. doi:10.1016/j.matpr.2022.06.298.

10. Rahman S, Sharme RK, Terrones M, Rana MM. Recent progress on layered Sn and Pb-based mono chalcogenides: synthesis, structure, optical, and thermoelectric properties and related applications. Nanomaterials. 2024;14(18):1530. doi:10.3390/nano14181530.
11. Tian XQ, Duan JY, Kiani M, Wei YD, Feng N, Gong ZR, et al. Hexagonal layered group IV–VI semiconductors and derivatives: fresh blood of the 2D family. Nanoscale. 2020;12(25):13450–9. doi:10.1039/d0nr02217a.
12. Deringer VL, Dronskowski R. Stabilities and reconstructions of clean PbS and PbSe surfaces: DFT results and the role of dispersion forces. J Phys Chem C. 2016;120(16):8813–20.
13. Deringer VL, Csányi G. Many-body dispersion correction effects on bulk and surface properties of rutile and anatase TiO_2. J Phys Chem C. 2016;120(38):21552–60. doi:10.1021/acs.jpcc.6b07141.
14. Zhang DN, Zhao L, Wang JF, Li YL. Electronic structures and the stability of MgO surface: density functional study. Surf Rev Lett. 2015;22(3):1550037. doi:10.1142/s0218625x15500377.
15. Soussi A, Haounati R, hssi Ait A, Taoufiq M, Asbayou A, Elfanaoui A, et al. First principle study of structural, electronic, optical properties of Co-doped ZnO. J Compos Sci. 2023;7(12):511. doi:10.3390/jcs7120511.
16. hssi Ait A, Soussi A, Labchir N, Taoufiq M, Najih H, Elfanaoui A, et al. A DFT theoretical and experimental study of the effect of indium doping within electrochemical deposited ZnO. Vacuum. 2023;217:112503. doi:10.1016/j.vacuum.2023.112503.
17. An X, Tian B, Deng Q, Ma H, Yuan W, He Z, et al. Promoted Na solubility and modified band structure for achieving exceptional average ZT by extra Mn doping in PbTe. ACS Appl Mater Interfaces. 2024;16(4):4827–35. doi:10.1021/acsami.3c17052.
18. Shi G, Wang H, Zhang Y, Cheng C, Zhai T, Chen B, et al. The effect of water on colloidal quantum dot solar cells. Nat Commun. 2021;12(1):4381. doi:10.1038/s41467-021-24614-7.
19. Geldasa FT, Dejene FB. Transition metal doping effects on the structural, mechanical, electronic, and optical properties of α-NiS for photocatalysis applications via DFT + U insights. Appl Phys A. 2025;131(11):869. doi:10.1007/s00339-025-08942-9.
20. Naziyev JY, Jafarova AN. Doping effect on electronic and magnetic properties of Ag-doped single-walled (6, 0) GaN nanotubes: first-principles study. Solid State Sci. 2024;149(5):107431. doi:10.1016/j.solidstatesciences.2023.107431.
21. Gomes AMC, da Silva MPC, Oliveira AF, Huanca DR. The role of Ag as-doping in modulating the band gap and interfacial properties of TiO_2/n-Si heterojunctions. J Phys Chem Solids. 2026;209(1):113311. doi:10.1016/j.jpcs.2025.113311.
22. Blaha P, Schwarz K, Tran F, Laskowski R, Madsen GKH, Marks LD. WIEN2k: an APW+lo program for calculating the properties of solids. J Chem Phys. 2020;152(7):074101. doi:10.1063/1.5143061.
23. Hohenberg P, Kohn W. Inhomogeneous electron gas. Phys Rev. 1964;136(3B):B864–71. doi:10.1103/physrev.136.b864.
24. Kohn W, Sham LJ. Self-consistent equations including exchange and correlation effects. Phys Rev. 1965;140(4A):A1133–8. doi:10.1103/physrev.140.a1133.
25. Perdew J, Burke K, Ernzerhof M. Generalized gradient approximation made simple. Phys Rev Lett. 1996;77(18):3865–8. doi:10.1103/PhysRevLett.77.3865.
26. Qureshi MT, Farooq U, Yunus G, Mohammed AM, Hussein AWMA, Rehman W, et al. DFT and experimental investigations on structural, electronic, thermoelectric, and optical properties of Zn doped PbS. Appl Phys A. 2025;131(4):240. doi:10.1007/s00339-025-08367-4.
27. Monkhorst HJ, Pack JD. Special points for Brillouin-zone integrations. Phys Rev B. 1976;13(12):5188–92. doi:10.1103/physrevb.13.5188.
28. Yoo SH, Todorova M, Wickramaratne D, Weston L, Van de Walle CG, Neugebauer J. Finite-size correction for slab supercell calculations of materials with spontaneous polarization. npj Comput Mater. 2021;7(1):58. doi:10.1038/s41524-021-00529-1.
29. Hofmann OT, Zojer E, Hörmann L, Jeindl A, Maurer RJ. First-principles calculations of hybrid inorganic-organic interfaces: from state-of-the-art to best practice. Phys Chem Chem Phys. 2021;23(14):8132–80. doi:10.1039/d0cp06605b.

30. Ahmed TY, Saeed SR, Aziz SB, Abdullah OG. First-principles investigation of substitutional metallic doping effects on the optical absorption of TiO_2 for photovoltaic applications. Oxf Open Mater Sci. 2025;5(1):itaf013. doi:10.1093/oxfmat/itaf013.
31. Tanisa NY, Rahman M, Musa AM, Bhuiyan JH, Aziz T. Comprehensive DFT study of structural, mechanical, dynamical, electronic, and optical properties of ZnX (X = S, Se, Te) semiconductors. Adv Mater Sci Eng. 2026;2026(1):2466402. doi:10.1155/amse/2466402.
32. Yasin Ahmed T, Aziz SB, Dannoun EMA. New photocatalytic materials based on alumina with reduced band gap: a DFT approach to study the band structure and optical properties. Heliyon. 2024;10(5):e27029. doi:10.1016/j.heliyon.2024.e27029.
33. Madsen GKH, Singh DJ. BoltzTraP. A code for calculating band-structure dependent quantities. Comput Phys Commun. 2006;175(1):67–71. doi:10.1016/j.cpc.2006.03.007.
34. Kang J, An Y, Xue J, Ma X, Li J, Chen F, et al. Density functional theory study of the electronic structures of galena. Processes. 2023;11(2):619.
35. Ramay SM, Aldosary MH. Investigation of structural, morphological, optical and electronic properties of Cu-doped PbS thin films: a comparative experimental and theoretical study. Phys Scr. 2024;99(8):0859a3. doi:10.1088/1402-4896/ad6519.
36. Dehdashti Jahromi H. Optical and electronic properties of lead sulfide spherical nano particle. Optik. 2021;231(1):166503. doi:10.1016/j.ijleo.2021.166503.
37. Mahraj I, Ptok A. First-principles investigations of structural, electronic and optical properties of ternary chalcopyrite semiconductors $CuInY_2$ (Y = S, Se and Te). Comput Condens Matter. 2024;40:e00935.
38. Zuñiga-Puelles E, Levytskyi V, Özden A, Gürel T, Bulut N, Himcinschi C, et al. Thermoelectric properties and scattering mechanisms in natural PbS. Phys Rev B. 2023;107(19):195203. doi:10.1103/physrevb.107.195203.
39. Cadavid D, Wei K, Liu Y, Zhang Y, Li M, Genç A, et al. Synthesis, bottom up assembly and thermoelectric properties of Sb-doped PbS nanocrystal building blocks. Materials. 2021;14(4):853. doi:10.3390/ma14040853.
40. Wang H, Gurunathan R, Fu C, Cui R, Zhu T, Snyder GJ. Thermoelectric transport effects beyond single parabolic band and acoustic phonon scattering. Mater Adv. 2022;3(2):734–55. doi:10.1039/d1ma00780g.
41. Chen Z, Cui HH, Hao S, Liu Y, Liu H, Zhou J, et al. GaSb doping facilitates conduction band convergence and improves thermoelectric performance in n-type PbS. Energy Environ Sci. 2023;16(4):1676–84. doi:10.1039/d3ee00183k.
42. Hou Z, Wang D, Hong T, Qin Y, Peng S, Wang G, et al. Boosting thermoelectric performance of n-type PbS through synergistically integrating in resonant level and Cu dynamic doping. J Phys Chem Solids. 2021;148:109640. doi:10.1016/j.jpcs.2020.109640.
43. Akhtar SEA, Neophytou N. Conditions for thermoelectric power factor improvements upon band alignment in complex bandstructure materials. ACS Appl Energy Mater. 2025;8(3):1609–19. doi:10.1021/acsaem.4c02747.